

Time domain optical imaging device based on a commercial time-to-digital converter

Cite as: Rev. Sci. Instrum. **92**, 103704 (2021); <https://doi.org/10.1063/5.0054516>

Submitted: 19 April 2021 • Accepted: 25 September 2021 • Published Online: 08 October 2021

 P. Pérez-Tirador,  K. I. Papadimitriou,  S. Powell, et al.



View Online



Export Citation



CrossMark

ARTICLES YOU MAY BE INTERESTED IN

[Design and implementation of DC-to-DC converter topology for current regulated lightning generator](#)

Review of Scientific Instruments **92**, 104709 (2021); <https://doi.org/10.1063/5.0060247>

[Simplified feedback control system for scanning tunneling microscopy](#)

Review of Scientific Instruments **92**, 103705 (2021); <https://doi.org/10.1063/5.0064511>

[On the use of field programmable gate arrays in light detection and ranging systems](#)

Review of Scientific Instruments **92**, 121501 (2021); <https://doi.org/10.1063/5.0049880>

Lock-in Amplifiers
up to 600 MHz



Zurich
Instruments



Time domain optical imaging device based on a commercial time-to-digital converter

Cite as: *Rev. Sci. Instrum.* **92**, 103704 (2021); doi: [10.1063/5.0054516](https://doi.org/10.1063/5.0054516)

Submitted: 19 April 2021 • Accepted: 25 September 2021 •

Published Online: 8 October 2021







View Online



Export Citation



CrossMark

P. Pérez-Tirador,^{1,a)}  K. I. Papadimitriou,^{2,b)}  S. Powell,^{3,c)}  and J. C. Hebden^{1,d)} 

AFFILIATIONS

¹ Department of Medical Physics and Biomedical Engineering, University College London, London WC1E 6BT, United Kingdom

² Department of Computer Science, University College London, London WC1E 6BT, United Kingdom

³ Department of Electrical and Electronic Engineering, University of Nottingham, Room 705 Tower, University Park, Nottingham NG7 2RD, United Kingdom

^{a)} Author to whom correspondence should be addressed: pablo.tirador.15@alumni.ucl.ac.uk

^{b)} k.papadimitriou@ucl.ac.uk

^{c)} Samuel.Powell@nottingham.ac.uk

^{d)} j.hebden@ucl.ac.uk

ABSTRACT

Time-domain diffuse optical imaging is a noninvasive technique that uses pulsed near-infrared light as the interrogation source to produce quantitative images displaying the variation in blood volume and oxygenation in the human brain. Measuring the times of flights of photons provides information on the photon pathlengths in tissue, which enables absolute concentrations of the oxygenated and deoxygenated forms of hemoglobin to be estimated. Recent advances in silicon electronics have enabled the development of time-domain systems, which are lightweight and low cost, potentially enabling the imaging technique to be applied to a far greater cohort of subjects in a variety of environments. While such technology usually depends on customized circuits, in this article, we present a system assembled from commercially available components, including a low-cost time-to-digital converter and a silicon photomultiplier detector. The system is able to generate histograms of photon flight times at a rate of 81–90 kS/s and with a sampled bin width of 54 ps. The linearity and performance of the system are presented, and its potential as the basis for a modular multi-detector imaging system is explored.

© 2021 Author(s). All article content, except where otherwise noted, is licensed under a Creative Commons Attribution (CC BY) license (<http://creativecommons.org/licenses/by/4.0/>). <https://doi.org/10.1063/5.0054516>

I. INTRODUCTION

The oxygenated and deoxygenated forms of hemoglobin have different optical absorption characteristics, and consequently, measurements of the transmission of near-infrared (NIR) light at two or more wavelengths across human tissue (such as a region of the head) can be used to monitor their relative concentrations. A combination of measurements made at multiple locations on the tissue surface enables images to be generated, which display the variation in blood volume and oxygenation in the underlying tissues. This approach, known as diffuse optical tomography (DOT), has been widely used to study the human brain and, especially, the response of the brain to sensory stimuli and cognitive tasks.^{1–3} Because the technology is both safe and relatively portable, DOT has been a popular tool for studying the developing brains of infants and babies. However, because the light is highly scattered, simple

measurements of transmitted intensity are insufficient to quantify absolute hemoglobin concentrations. This limitation can be overcome if the distances traveled by the photons in the tissue are measured, and this can be achieved using ultrafast technology, which records the flight times of photons with a picosecond resolution. Until recently, such technology has been very expensive, bulky, and power-consuming.³ In addition, most systems developed over the past 20 years have employed optical fibers or fiber bundles to couple sources and detectors to the scalp. Imaging over an entire scalp typically requires around 20–30 discrete source positions (emitting at two or more wavelengths) and a similar number of detector positions.

Photonic devices are now available that make it possible to measure photon flight times using systems that are lightweight, low cost, and potentially wearable, i.e., small enough to place directly in contact with the scalp, precluding the need for optical fibers.^{2–4} These

systems employ solid-state [single photon avalanche diode (SPAD) and especially SiPM] detectors, which operate at much lower voltages than photomultiplier tubes (PMTs) used in earlier DOT instruments and are smaller in size, and a time-to-digital converter (TDC), a device that measures the time interval between two events and converts it into a digital output. Designs have adopted two different approaches: either modular systems that divide the signal chain into separate components (usually with the TDC separate from the sensor) or those that integrate sensors and signal processing units on the same integrated circuit.

A broad variety of modular systems have been developed. Researchers at the Physikalisch-Technische Bundesanstalt (Berlin) have demonstrated a noncontact DOT system based on SPAD technology,^{5,6} while investigators at the Martinos Center for Biomedical Imaging (Boston) have evaluated a CCD camera-based DOT system⁷ and a skin contact-sensitive probe, which reduces error due to variation in the optical coupling.⁸ Systems based on SPADs and SiPMs have been pioneered by a research team at the Politecnico di Milano, who have described several modular DOT devices, typically involving a sensor and solid-state source embedded within a flexible probe held in contact with the head. For example, they have presented a SiPM-based detection module with temperature control,⁹ a coin-sized laser source with a custom CMOS 1 MHz driver,¹⁰ and a SiPM probe with an amplification system that fits on a cap (validated on phantoms and human volunteers).¹¹ More recently, they have demonstrated a two-channel system that fits into a 5U rack box and integrates eight sources (at 40 MHz repetition rate and milliwatt power), two SiPMs, and two independent TDCs (custom ASIC, 10 ps resolution), all coordinated with an FPGA that can generate histograms in real time.^{12,13} Other modular DOT probes include the LinoSPAD, described by Burri *et al.*,¹⁴ which combines a SPAD with a FPGA-based TDC (that implements up to 64 channels with 50 ps resolution at 80 MS/s), and those described by Saha *et al.*^{15–17} that integrate a vertical-cavity surface-emitting laser (VCSEL) source with user-tunable pulse characteristics (providing a power of ~2 mW and a pulse rate of up to 100 MHz), a time-gated SiPM or a SPAD, and a custom-designed chip that serves as the TDC (achieving a temporal resolution of around 30 ps) and signal processing units. The first commercial time-domain DOT system based on an array of 52 modular, wearable probes, which incorporate laser diode sources, sensors, and TDCs, was recently announced by Kernel.¹⁸ It is claimed that this system is capable of streaming data through a universal serial bus (USB) connection from over 1500 source–detector pairs at 200 Hz and combines optical data with electroencephalography (EEG).

Integrated devices, where sensors and timing electronics are combined on the same silicon die, generally employ SPADs rather than SiPMs due to their cheaper manufacture.^{19,20} Such devices include the NIROT chip described by Pavia *et al.*,²¹ which implements 100 TDCs with a sample processing time of 5 ns and has been validated on tissue-equivalent phantoms, and the Ocelot system,²² which consists of 1728 TDCs and has been designed primarily for LIDAR applications. Both devices achieve a temporal resolution of about 50 ps and implement a 3D structure in silicon to reduce the overall volume. Meanwhile, line sensors developed for multispectral imaging, reported by Erdogan *et al.*,^{23,24} consist of rectangular arrays of varying size with one TDC per pixel, with an adjustable bin resolution per TDC and multiple modes of operation (single photon

counting and in-device histogramming). This device has demonstrated sample rates of the order of GS/s. More recently, devices that integrate multiple SPADs in a single SiPM-like structure have been described. A system reported by Nolet *et al.*²⁵ combines TDCs with 10 ps resolution and a readout ASIC that compensates for timing differences in each SPAD to provide a 256 element array for positron emission tomography (PET) applications. Finally, Conca *et al.*²⁶ have demonstrated a gated digital SiPM with integrated CMOS TDC, which integrates a 78 ps resolution histogram builder for TD-NIRS applications.

The development of customized integrated circuits for the time-to-digital conversion and signal conditioning is expensive, both financially and in terms of effort. Dependence of DOT systems on such units therefore limits the capacity to replicate, maintain, and update them. However, while the commercial DOT market is relatively modest, miniaturized time-of-flight technology is being widely developed for much broader applications, such as range sensing for LIDAR and the auto-focus of digital cameras. In Secs. II–IV, we report an exploration of the use of inexpensive, widely available integrated circuits as the basis of a portable, modular time-domain DOT device.

II. SYSTEM DEVELOPMENT

A. Design and primary components

The objective of the work reported here was to demonstrate a time-domain DOT technology, which could ultimately be implemented on a small wearable module, incorporating one or more sources, detectors, and the signal conditioning and timing circuitry. The purpose was to acquire histograms of photon flight times (commonly known as temporal point spread functions or TPSFs) for each source–detector pair, which may then be analyzed offline to generate localized measures and/or reconstructed images of tissue optical properties and/or physiological parameters.

All aspects of the system design were determined on the basis of low cost, small footprint, and easy replication. The design should be modular to support any number of detectors operating in parallel, and the only external components should be a central control unit, a power supply, and (at the present stage of development) a fiber-coupled laser source.

We elected to base our system on a SiPM detector and a low-cost commercially available TDC. SiPMs generally offer good sensitivity to NIR light over a small area coupled with a fast (sub-nanosecond) response time. We selected the On Semiconductor/SensL MicroFC-10010 silicon photomultiplier with a 5% sensitivity over a square $1 \times 1 \text{ mm}^2$ area, producing pulses with a 0.3 ns rise time. While an attractive alternative to high-voltage PMTs, the breakdown voltage for SiPMs can still be high (27 V in this case), which means they must be carefully insulated. We also utilized a MicroFC-SMA-10010 board from the same manufacturer during the system development, which provides convenient SMA connections to the SiPM.

The Texas Instruments TDC7201 is a small footprint ($4 \times 4 \text{ mm}^2$) integrated circuit developed for LIDAR and ultrasound applications but with characteristics that make it attractive as a TDC for a modular DOT system. This IC provides two independent oscillator-based TDC channels that measure the time between a “start” pulse (in this case, a photon event) and a reference

“stop” pulse (the sync signal from the laser). The TDC7201 has a quoted temporal resolution of ~ 55 ps with a measurement uncertainty of 35 ps and can be connected to an external controller through a serial peripheral interface (SPI) with one common input line (MOSI) and two separate outputs (MISO) for the device setup and data retrieval. The sampling rate for this device is not specified in the datasheets and was characterized experimentally. Development was aided by the TDC7201-ZAX-EVM test board, which includes 50 Ω -terminated SMA inputs, an 8 MHz oscillator driving the measurements, and SPI and pins for the control interface.

We implemented the data retrieval and coordination with reconfigurable hardware on an FPGA. This approach makes the sampling process more efficient than a traditional microcontroller, as fast hardware resources can be dedicated to histogram memory and to building a lightweight system controller. By using reconfigurable ICs, such as an FPGA, a design that works with a single channel can be replicated multiple times, including many instances on the same circuit.

Our system was implemented on a Xilinx Artix 7 FPGA using the Nexys 4 DDR development board from Digilent Inc. This is an entry-level board that provides six generic input/output ports via a PMOD interface, LEDs and buttons for control and debugging, and an FTDI serial-over-USB interface. This was connected to the TDC test board through an adaptor board.

The connection protocols should be easy to maintain. In the system presented here, all connections are performed using either transistor-transistor logic (TTL) pulses or via a serial USB stream. Software development focused on data acquisition only, with all processing assumed to be performed offline, and Python was chosen as a programming language for its simplicity and portability.

During development and evaluation of the system, two different external laser sources were used. For initial functionality tests, we employed an IMRA Femtolite A-15 single wavelength pulsed fiber laser (780 nm) with a repetition rate of 48 MHz. A filter was used to reduce the output to eye-safe (<1 mW) power, and a synchronization signal was generated by using an optical beam splitter to illuminate a photodiode (Thorlabs DET025). For experiments on tissue-equivalent phantoms, an NKT SC400 supercontinuum laser combined with acousto-optic tunable filters (AOTFs) was used, which provides picosecond pulses at a 40 MHz repetition rate at a user-tunable wavelength in the range of 410–2400 nm. This source is described in detail by Cooper *et al.*²⁷

B. Signal conditioning

Signals produced by the SiPM and photodetector (for event detection and synchronization, respectively) are weak (close to the electric noise floor) and vary in amplitude. To be used as timing inputs for a TDC, such signals need to undergo signal conditioning, consisting of three stages: amplification, thresholding, and pulse shaping (yielding pulses with a constant amplitude and width).

Signal amplification was achieved using Mini-circuits block amplifiers (ZFL-500+ and ZFL-1000+), which output signals with a peak amplitude of around 100 mV and with a pulse width of about 5 ns. Smaller radio frequency (RF) amplifiers are also a viable option. Thresholding and pulse shaping circuitry was developed on a single 100×100 mm² board, including voltage regulators and a

multichannel DAC to externally adjust the thresholds and configuration voltages via a serial interface. A fixed threshold is applied to the signal using a MAX9600 NECL comparator. This is a fast comparator (<1 ns rise time) with good sensitivity to low-voltage signals and provides an additional hysteresis adjustment (via a potentiometer) that controls how the IC output switches in response to a rapidly changing input.

Although, after amplification, the noise amplitude can sometimes be as large as the pulses from the photodetectors, by setting the input threshold above the usual noise floor and adjusting the hysteresis, most of the noise can be avoided. The variability of the input and the effects of hysteresis cause variability in output pulse duration, and therefore, pulse shaping is applied to obtain stable pulses at a desired amplitude and duration. Pulse shaping is easily and commonly performed using a flip-flop circuit with feedback on the reset input, where the pulse width depends on the length of the feedback transmission line. However, to obtain a smaller, more integrated solution, we employed a circuit consisting of two LTC6752 TTL comparators setup in a one-shot multivibrator configuration. The pulse width is then 5 ns (the minimum output duration of the IC) if the input pulse is very short or the timing constant of an RC subnet. If the input pulse width is suspected to be too short, a third LTC6752 can be employed in an intermediate stage to produce 5 ns pulses. The operation of this pulse shaping configuration depends on the input thresholds of the comparators, which were manually set, depending on the experiment. To enable adjustment of the amplitude and minimize losses when connecting to a 50 Ω line, an operational amplifier was added to the final stage of the conditioning circuit. The circuits, including the values for the resistors and capacitors, were designed with the aid of a simulation with LTspice. [Figure 1](#) shows a schematic of the comparator and pulse shaping circuit.

C. The FPGA

The FPGA was programmed to configure the TDC7201, retrieve the event times, assemble time-of-flight histograms, and communicate with a personal computer (PC). As illustrated in [Fig. 2](#), this is achieved via connection to a clock cycle counter that keeps track of the integration time, an SPI driver, the histogram memory, and a control unit. Note that all operate independently so that the timing of one component is not affected by the operation of the others.

The histogram memory consists of an array of 24-bit registers, where a given bin in the histogram is updated when an event is registered by adding one to the corresponding memory location. This memory can be implemented using the fast RAM internal to the FPGA, which comes in blocks of synchronous 36 Kb memory cells, meaning that the TPSFs can be generated on the fly without needing to store all incoming events at a fast rate. The primary limitation of this implementation is that the measurement range of the TDC7201 (24 bits, $2^{24} \approx 1.7 \times 10^7$ values) quickly exhausts the memory resources of the FPGA. The repetition rate limits the time range during which detected events can occur to 25 ns for a 40 MHz repetition rate (equivalent to ~ 455 bins of 55-ps width), so the system can be implemented with a more limited number of bins. The system was developed with 768 bins (equivalent to a range of ~ 42 ns), which accommodates the laser repetition rate while providing capacity for experimentation with alternative sources.

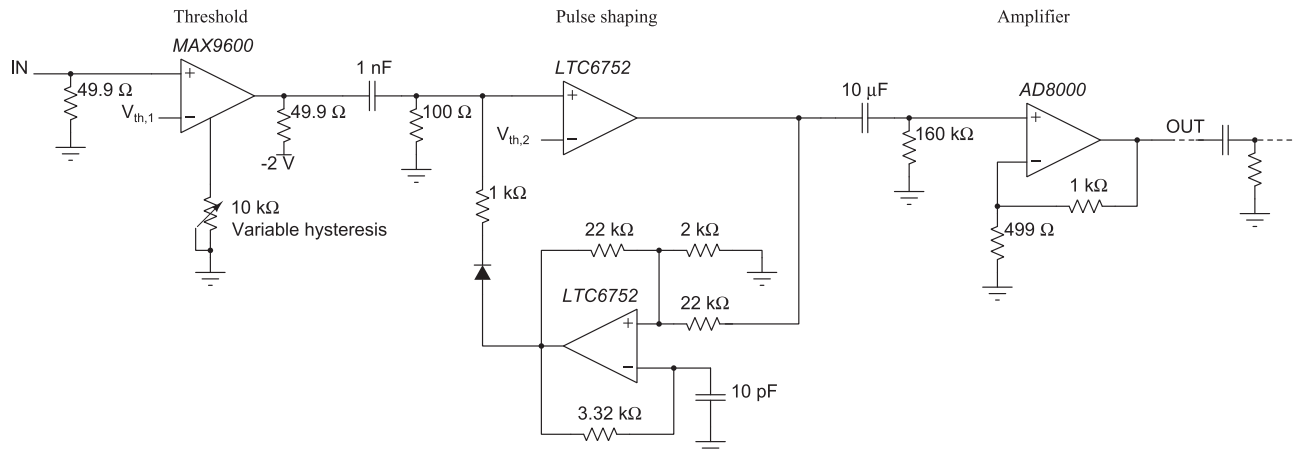


FIG. 1. Simplified schematic of the comparator circuit, including the thresholding, pulse shaping, and final amplification. In the physical board thresholds, $V_{th,1}$ and $V_{th,2}$ are set manually with an ADC. The output can be passed through a DC filter if necessary.

The Xilinx PicoBlaze soft microcontroller was used to coordinate the operation of all the components. This is a simple low-resource 8-bit microcontroller without peripherals that can be freely used with Xilinx devices and is distributed with its VHDL code. This makes the task of programming the steps of the acquisition process more flexible and easier to modify than using a complex state machine while keeping the resource use in the FPGA low. The program is written in PicoBlaze assembly code, which is comprised of simple, easy to read instructions. Its customizability in VHDL allowed it to be automatically connected with custom peripherals that had been already written, such as the histogram memory. The main acquisition loop, where most of the changes are done, is short, which makes maintenance easy.

The TDC7201 is configured to detect the rising edge of pulses, to calibrate for the minimum number of cycles to keep the response time short, and to measure the time of flight in *mode 1*, which allows measuring times between 12 and 2000 ns sufficient for the TPSFs.

To record a time of flight, the controller starts the TDC and waits for an interrupt. The time can be reconstructed from the contents of three 24-bit registers: one containing the result of an internal counter representing the measured time and two containing a time calibration value (ns/bin). The calibration value was found to vary by less than 100 fs over a period of several minutes, and therefore, to accelerate the readout process, only the counter measurement is read every event, and the calibration is retrieved just once per experiment. The data are routed to the histogram memory, and from the memory to the serial link, without passing through the microcontroller, avoiding costly 8-bit operations.

A PC controls the data capture process, signaling the FPGA to start the measurement, and store the incoming data. Following the acquisition, PC software is used to correct for the nonlinearities of the system (see Sec. IV A 4) and display and analyze the TPSFs.

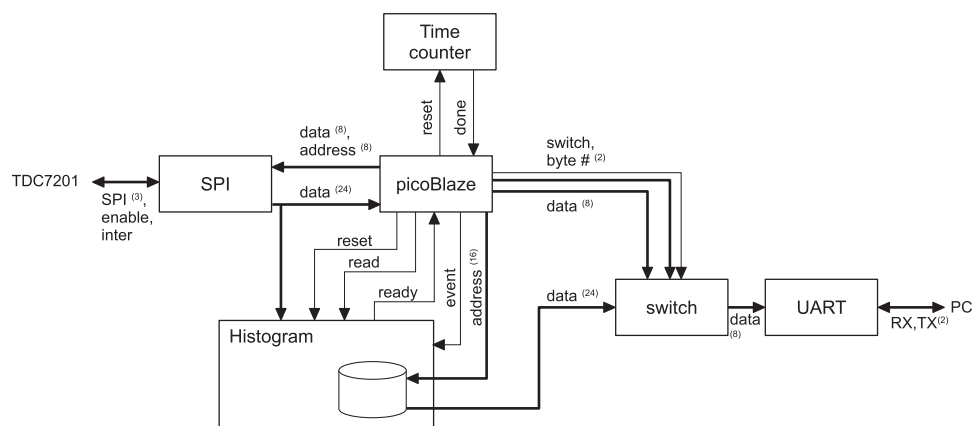


FIG. 2. Schematic of the FPGA circuit for the single channel system. The small numbers represent the number of bits in a bus.

D. Expanding into a multichannel system

The TDC7201 provides two independent channels but only one MOSI line. This means that two sets of independent configuration instructions or register requests cannot be sent at the same time. While it is not possible to request registers to one channel if the communication with the other has already been started, it is still possible to request a read operation on the same register of both channels simultaneously. Because of the low probability of events arriving at both channels at the same time, this configuration does not improve the count rate with respect to doing a sequential check on the status of the channels, provided that both channels are polled regularly (i.e., the frequency at which one channel is checked should not obstruct the program from polling the other). In all cases, the total count rate is divided between the two channels. The sequential dual channel system implemented on the FPGA is illustrated in Fig. 3.

Another issue, which arises when implementing a dual channel configuration, is the routing of the sync signal to more than one load. Using independent comparators for each channel proved to be unreliable, as it becomes harder to discriminate between noise and the weak signal from the sync preamplifiers. A more effective solution is to branch the output and use different load configurations or buffer circuits to adjust for impedance mismatches.

The data acquisition system described here has the potential to be expanded to accommodate multiple TDC7201 chips. By reducing the memory resources of the FPGA to just 768 bins, the Artix 7 FPGA potentially has the capacity to host up to 30 simultaneous dual channel histogram memories (ignoring the additional resources needed to coordinate the PC communications). With the eight I/O ports available on the FPGA development board, up to three test boards can be connected at the same time. However, integrating multiple simultaneous detectors into the system also requires an appropriate time synchronization scheme to establish a common time base for every histogram (i.e., establishing a fixed point relative to the time at which the laser pulse is emitted). For a two-source,

two-detector system, this can be achieved by directly coupling each source to each detector (i.e., a total of four calibration measurements). However, this method becomes impractical for much larger numbers of pairs. For more complex systems, this problem can be solved by co-locating each source with a detector and employing back-reflection measurements²⁷ or by using common external synchronization signals.¹⁷

To reduce external electromagnetic (EM) interference, all circuits were shielded within aluminum boxes. When required, time delays were generated by changing the lengths of cables between components, as commercial delay units were found to introduce additional noise.

III. EXPERIMENTAL METHODS

Experimental evaluations of the system and its components were performed throughout the development using three basic configurations.

First, to test the functionality of the TDC, a function generator was employed, which provided two pulse trains at a frequency of up to 20 MHz and with an arbitrary phase shift between them. These were applied directly to the TDC7201.

Second, for assessing linearity, the free-space beam emitted by the IMRA Femtolite laser was aligned with the SiPM mounted on a translation stage within an enclosure to prevent detection of other sources of light. The beam was attenuated as required using neutral density filters.

Third, to evaluate the potential of the system to acquire TPSFs on human tissue, measurements were performed on a phantom with tissue-equivalent optical properties, as shown in Fig. 4. For such measurements, a variety of mechanical probes were 3D printed to accommodate either one or two SiPM test boards and support one or two source fibers coupled to the NKT laser/AOTF source. As illustrated in Fig. 4, the lower surface of the probe contains apertures for the detectors and the sources, which is then placed in contact with

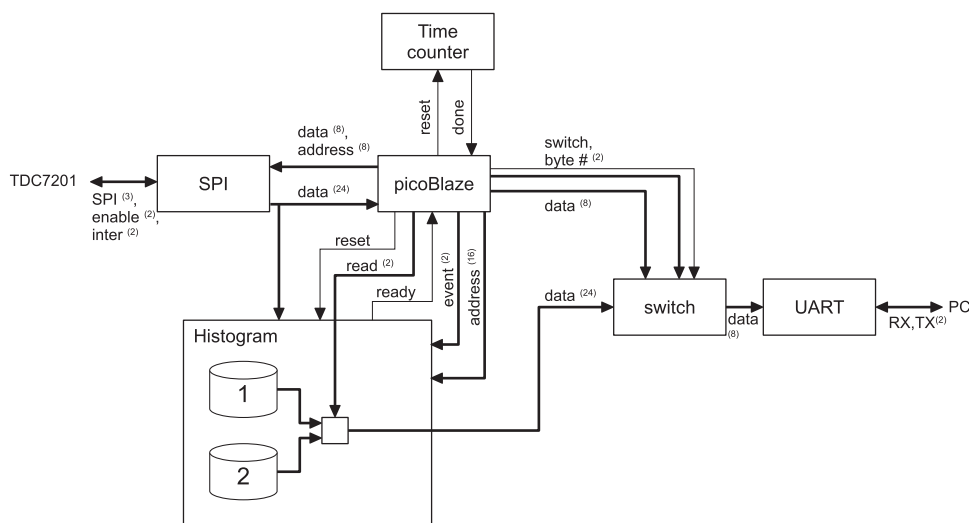


FIG. 3. Schematic of the FPGA circuit for the dual channel system. The small numbers represent the number of bits in a bus.

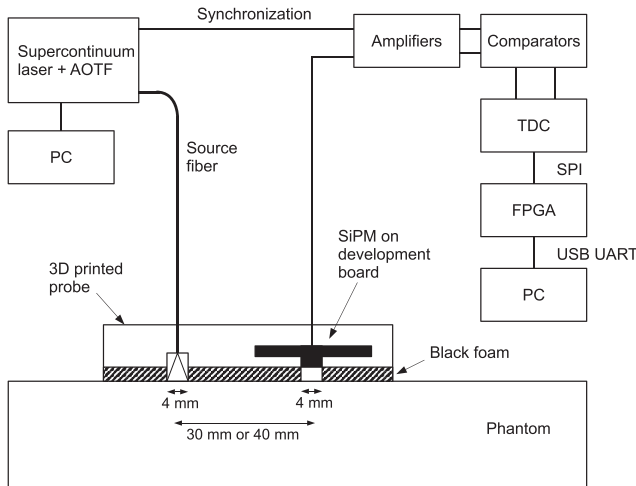


FIG. 4. Schematic of the experimental setup.

the phantom. The end of each source fiber was held a few millimeters above the lower surface of the probe to enable the divergence of the beam to illuminate a circular aperture of 4 mm diameter. Probes were fabricated with different fixed source–detector separations (30 and 40 mm). To prevent stray light reaching the detector(s), a 10 mm layer of soft black foam was added to the lower surface.

The phantom consisted of a solid rectangular block (dimensions $129 \times 190 \times 40 \text{ mm}^3$) cast from polyester resin mixed with titanium dioxide particles and NIR dye to provide a transport scattering coefficient of $\mu'_s = 1.00 \text{ mm}^{-1}$ and an absorption coefficient of $\mu_a = 0.01 \text{ mm}^{-1}$ at a wavelength of 800 nm. Embedded inside the block were two rows of four cylindrical targets (length of 10 mm and diameter of 10 mm). The targets have an absorption coefficient $5\times$, $10\times$, $20\times$, and $50\times$ that of the slab and were embedded at two different depths from the surface, 10 and 20 mm. A schematic of this phantom is shown in Fig. 5.

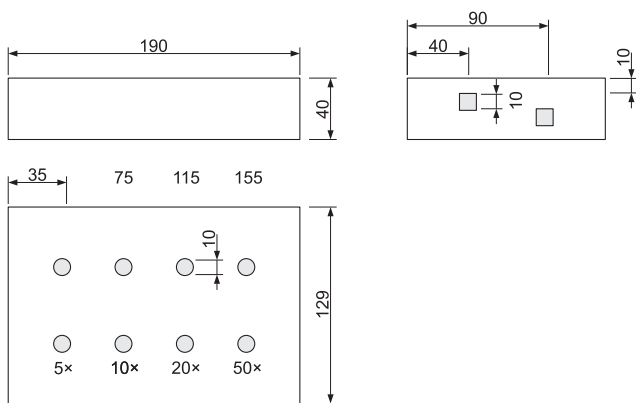


FIG. 5. Schematic of the phantom. The labels mark the relative absorption of each target.

For phantom experiments, separate measurements of the system impulse response function (IRF) were acquired at regular intervals by coupling the source fiber(s) directly to the SiPM(s) using neutral density filters to attenuate the source intensity.

For the second and third configurations, the signals from the SiPM and the synchronization photodiode are fed into an amplifier chain and then to the comparator board.

IV. RESULTS

A. System performance

A series of functionality tests were performed to characterize the performance of the prototype time-domain system, and the results are presented below. During these experiments, the bin size reported by the TDC was $\sim 54 \text{ ps}$.

1. Count rate limit

The TDC7201 datasheets and online documentation do not specify an upper limit for the event count rate, and therefore, it was established experimentally using a function generator to produce pulses at an adjustable rate. The frequency of the “start” signal was incremented in steps of 10 kHz over a 0–1 MHz range, while the “stop” frequency was fixed at either 6 or 15 MHz. The event count rate is shown plotted against the start pulse frequency in Fig. 6. The count rate linearity can be defined as a change in the measured event count rate per unit change in the true frequency. As the true count rate increases from zero, the measured count rate exhibits a linearity of one until it reaches a maximum, above which the rate immediately falls to half the maximum and then increases with a linearity of one-half. On reaching the maximum again, the measured count rates then fall by approximately one third and then increase with a linearity of one third, and so on. Thus, the count rate linearity is given by

$$\text{slope} = \frac{1}{n + 1}, \text{ where } n = \left\lfloor \frac{\text{count rate}}{\text{max count rate}} \right\rfloor. \quad (1)$$

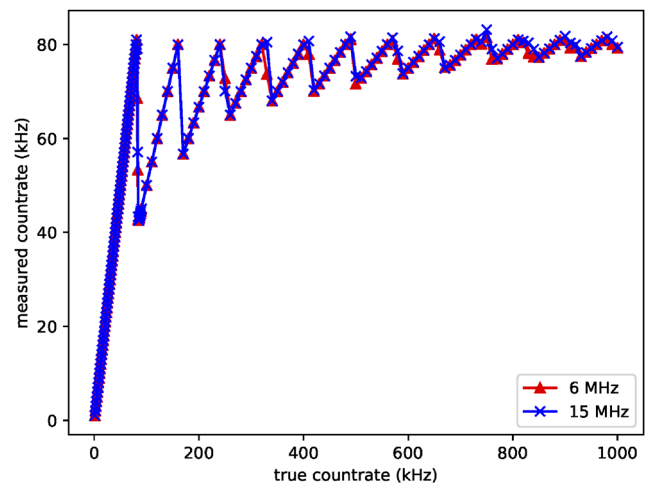


FIG. 6. Measured count rate of the system plotted against the input count rate for two different “stop” frequencies.

The observed behavior is caused by “pileup,” when the TDC receives an event signal before it has fully processed the previous event and is therefore unable to respond—any new events arriving after the “stop” signal and before the measurement status is reset are ignored. It is essential to ensure the true event rate remains below the maximum in order to obtain TPSFs, which are undistorted by the consequences of pileup. For both “stop” frequencies, the maximum count rate was observed to be ~ 81 kHz. However, some degree of dependence on the “stop” frequency was observed with a maximum count rate of about 90 kHz noted when the “stop” frequency was increased to 40 MHz.

2. Temporal stability

The time-of-flight technology is prone to jitter, which is high frequency (>1 Hz) and usually random instability, and temporal drift of the time base due to thermal effects, which largely disappear when the system reaches a constant temperature. Both phenomena were investigated by illuminating a SiPM with the IMRA laser beam

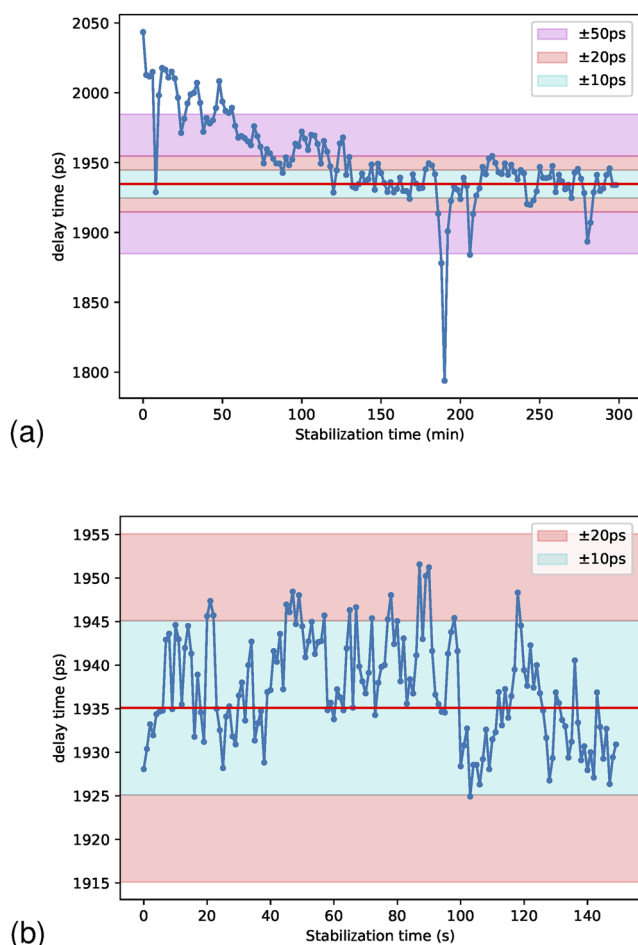


FIG. 7. The above graphs show the (a) stability and long-term drift and (b) short-term variation (*jitter*) of the system. The colored bands represent a range of ± 10 ps (blue), ± 20 ps (red), and ± 50 ps (magenta) with respect to the average mean time after 200 min (long term) or the mean of the full acquisition (short term).

and acquiring a measurement of the IRF for 1 s every 5 min for 5 h (beginning immediately after the entire system is switched on). After 5 h, another series of IRFs were acquired: for 1 s every 2 s for 5 min. The mean photon arrival time was estimated from each IRF. The values obtained over the 5-h period are shown in Fig. 7(a), and the values obtained over the subsequent 5-min period are shown in Fig. 7(b). It is evident that significant drift occurs over the first 2 h, after which the change in mean photon arrival time is dominated by jitter, which has a peak-to-peak variation of about 30 ps. A few large-amplitude spikes appear in these data, almost certainly due to external electromagnetic interference, which was minimized by isolating the TDC and signal conditioning circuitry within aluminum boxes. This experiment was repeated in less ideal circumstances with additional equipment operated in the vicinity, and the peak-to-peak jitter was observed to increase to about 60 ps.

3. Temporal linearity

When the SiPM was moved away from the laser in steps of 2 mm, average photon flight times derived from the IRFs were used to estimate the translated distances. The mean, maximum, and minimum of these estimates are plotted against the true distance in Fig. 8. Although the trend is highly linear, the data acquired at the positions closest and furthest from the laser (where the beam power is strongest and weakest) depart significantly from the trend. It is also observed that the range of values (maximum–minimum) is about 3.3 mm on average, which is significantly larger than the step size. This range of variation is a consequence of jitter; the maximum observed variation in distance is 20 mm, equivalent to 60 ps of time variation, which is consistent with the maximum jitter recorded in other experiments.

4. Differential nonlinearity

A so-called uniform density test was performed to assess the degree of nonuniformity in the width of the TDC histogram bins. The TDC is provided with a random series of pulses such that the

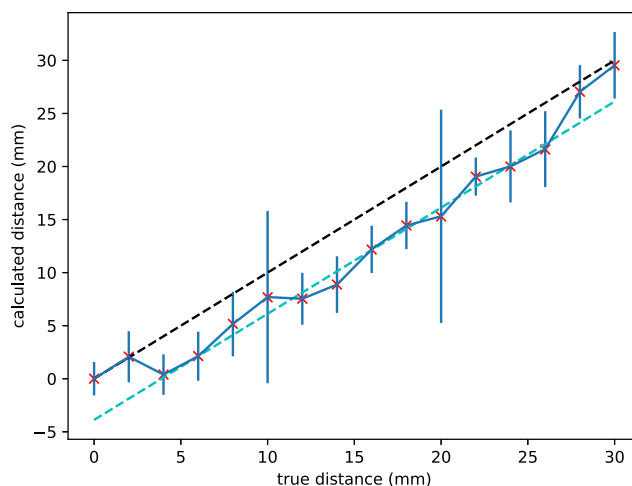


FIG. 8. Plot of the mean, maximum, and minimum estimated distance from a displacement experiment in free space. The dashed lines represent a slope of 1 with different offsets.

ideal histogram is flat, and any deviations can be attributed to non-linearities in the TDC or in the signal chain. The differential nonlinearity (DNL) codifies these deviations as a number between -1 and $+\infty$ and can be used to define a correction coefficient for each bin n as $C_n = 1/(1 + DNL_n)$. The corrected number of counts for bin n is therefore

$$N_{n,correct} = N_n \times C_n = \frac{N_n}{1 + DNL_n}. \quad (2)$$

Figure 9 shows the histogram, DNL, and correction factor C for a uniform density test performed using the SiPM as a source of random events (due to dark counts or a low level of continuous illumination). Because the DNL might vary due to changes in the electrical conditions of the system, the test should be performed each time the system is employed.

5. Comparison with a commercial TCSPC card

A Becker & Hickl SPC-130 TCSPC card was used during the testing of the system as a reference for the response of the detector and signal conditioning. Table I shows a comparison of timing characteristics between the full system as described in Secs. II and III, and the test system comprised of the SiPM, the signal conditioning board, and the TCSPC. The main differences between the two systems are the count rate, the jitter, and the DNL. The difference in jitter can be attributed to the greater robustness of the inputs for the SPC-130 card, while the count rate and the DNL depend more on the characteristics of the TDC. Other differences can be ignored—the difference in the FWHM of the IRF could be due to jitter and the difference in temporal drift could be due to the external factors in the setup of the stability experiment, which are difficult to maintain fully static for hours.

B. Imaging experiments

A simple image of the phantom was obtained by manually translating the single-SiPM probe with a 40 mm source-detector

TABLE I. Comparison of characteristics between the full system using the TDC7201 and another using a Becker & Hickl SPC-130 TCSPC.

	TDC7201 system	SPC-130 system
Maximum count rate (S/s)	$\sim 91 \times 10^3$	$\sim 1 \times 10^6$
Dark count (photons/s)	~ 2700	~ 3000
FWHM of IRF (ps)	~ 230	~ 200
Temporal drift (after 2 h) (ps/h)	~ 15	~ 12
Jitter (ps)	$\sim 30-60$	~ 20
DNL (peak-to-peak)	1.47 LSB	Negligible

separation across the phantom surface and acquiring TPSFs at a series of discrete positions. These positions were arranged in five rows, 16 mm apart, with 15 positions separated by 10 mm along each row. The source-detector axis was aligned perpendicular to each

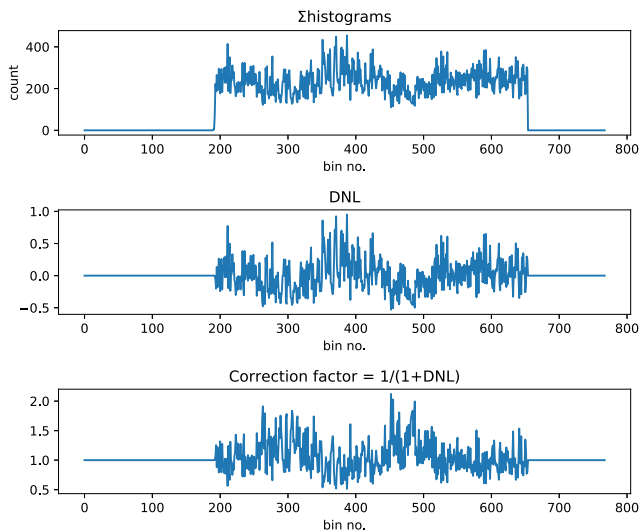
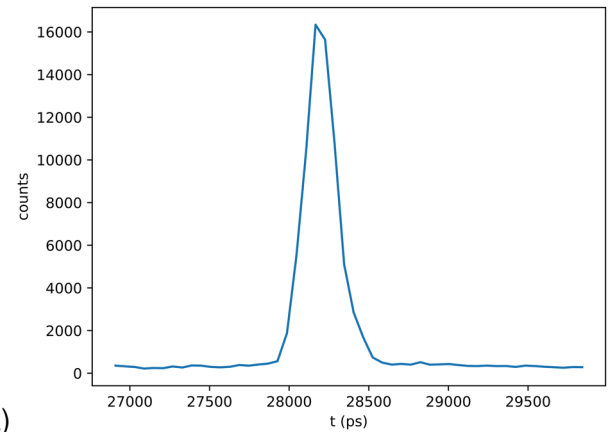
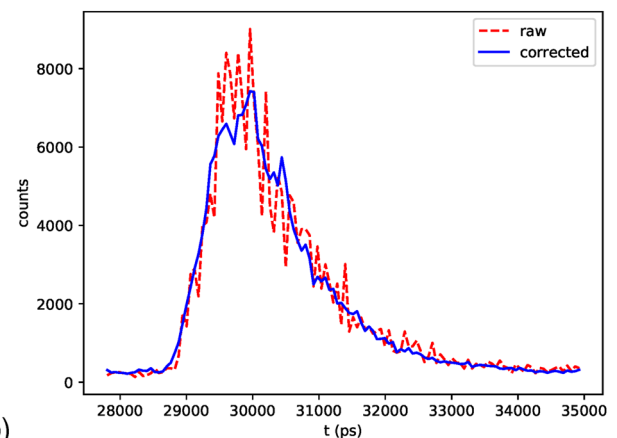


FIG. 9. Plot of a noise histogram and the DNL and the correction factor derived from it as acquired during an experiment with phantoms.



(a)



(b)

FIG. 10. Graphs showing (a) the IRF and (b) one of the TPSFs (before and after applying DNL correction) obtained during a raster scan of the central area of the phantom.

row. At each position, 20 TPSFs were collected, each corresponding to an exposure time of 1 s. The source consisted of a beam of picosecond pulses at a wavelength of 780 nm and a repetition rate of 40 MHz. The power emitted on the surface of the phantom was ~ 5 mW. Each set of 20 TPSFs was added and corrected using the DNL factors. Immediately following the phantom scan, the source fiber and SiPM were coupled on either side of a high-ND filter to acquire a measurement of the system IRF. The summed TPSFs were processed to obtain measurements of the photon count (intensity) and mean photon flight time for each position. The mean time of the IRF was subtracted from TPSF mean times to provide measurements of the absolute delays. The IRF and a typical example of a TPSF obtained during the experiment are shown in Fig. 10.

Figure 11 shows maps of the variation in intensity and mean time across the surface of the phantom, measured at the 75 discrete positions. The positions of the embedded targets are indicated by red dots. The top row of targets are at a depth of 10 mm below the surface, and the bottom row are at a depth of 20 mm, with the absorption of the targets increasing from left to right as indicated in Fig. 5.

As expected, when the probe is positioned directly above a target, the detected intensity is lower, and the contrast is greater for the top row, where the targets are more superficial. It is also evident that the ability to spatially resolve the targets is superior along the horizontal direction than in the vertical direction, which is due to the fact that the source and detector are aligned vertically (i.e., the sampled

volume is elongated along the direction perpendicular to the rows of targets).

The map generated from the mean-time values is noisier. The positions of the targets in the top row clearly correspond to regions of larger mean time, implying that longer flight-time photons are less likely to be absorbed by the targets than shorter flight-time photons. Thus, many of the received photons at these positions have evidently traveled beneath the shallow targets, and the effect is greatest where the target absorption is greatest (on the right). This trend is reversed in the bottom row of deeper targets, where the mean time evidently decreases as the target absorption increases. This is because the longer flight-time photons are more likely to reach and be absorbed by the deeper targets than the shorter flight-time photons. This effect and its underlying cause were later confirmed using a Monte Carlo simulation of the experiment.

V. DISCUSSION AND CONCLUSIONS

In this article, we have presented a prototype time-domain imaging system assembled from off-the-shelf components and demonstrated the level of performance that can be achieved compared to more complex or expensive systems. The TDC, SiPM, and FPGA are all readily available at low cost, and the comparator circuit is easily built from basic electronic components. The primary feature of this design strategy is modularity, which allows elements to be substituted with alternatives while keeping the rest of the system intact. This offers benefits such as scalability, customization to the specific needs of the user, and straightforward update of components offering improvements in sensitivity, temporal resolution, linearity, maximum count rate, or price. Dissociating the TDC from the data acquisition hardware could also be helpful for testing new acquisition schemes and to reuse the TDC7201 in other systems, which could benefit from it. In addition, the accessibility of the components and materials and the flexibility of the design have the potential to expand the appeal of the time-domain approach for DOT applications, especially for developers with limited fabrication resources.

Compared to other contemporary time-of-flight systems, the temporal sampling interval of the TDC7201 (54 ps) is similar to many (although coarser than the latest ASIC-printed TDCs), as is the observed jitter. However, the DNL recorded for the whole system (not just due to the TDC) appears larger than some systems described in the recently published literature, and the maximum count rate of our prototype is significantly lower than most due to the characteristics of the TDC circuit. The number of counts can also be increased by increasing the integration time, and the base oscillator frequency on the TDC can be raised from 8 to 16 MHz. The DNL and overall noise can be reduced by placing the whole signal chain, including the TDC, within the same printed circuit board (PCB) and reducing the number and length of cabled connections. This would improve the portability as well as the stability of the system. In the future, other elements such as temperature control can be introduced to improve the stability and time synchronization routes to automate the time calibration process. Another step that can be taken with this architecture is implementing the TDC inside the FPGA, exploiting the delay of internal elements. These structures are capable of count rates of the order of MS/s with tens of picoseconds of resolution and are being used for

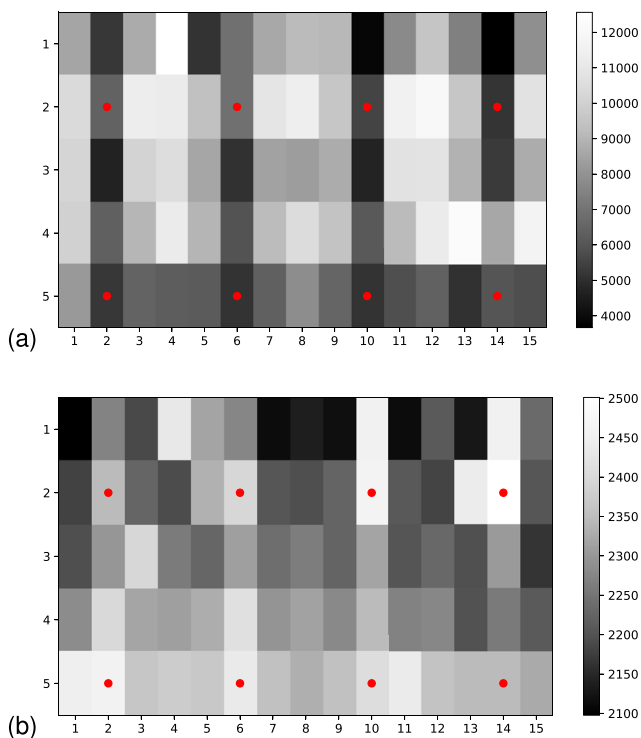


FIG. 11. Raster scan of the central area of the phantom showing for each position (a) the intensity (photons/s) and (b) the mean time of flight (ps). The red dots mark the positions of the targets. Data for the position (1, 6) were interpolated.

photon counting.¹⁴ Once problems with electrical connections are solved, a system based on this principle is ready to be tested on phantoms.

Phantom experiments reveal that the system characteristics are sufficient to record changes in intensity and time of flight associated with localized changes in absorption and thus enable simple maps of the variation in these data to be generated. The next step following this is to calculate absolute maps of μ_a and μ'_s , for which the dual channel system will provide three dimensional data. Future work will concentrate on *in vivo* measurements at two or more wavelengths and expansion to a modular, multi-detector system. The regions sampled by each source–detector pair must necessarily overlap to facilitate 3D imaging of the interrogated volume.

Achieving a wearable, modular system will require a fully portable source, ideally without the need for optical fiber coupling. A promising source technology, which has already been demonstrated for this application, is the VCSEL (e.g., Saha *et al.*^{15–17} and Papadimitriou *et al.*²⁸), which can provide picosecond pulses at selected near-infrared wavelengths and can be directly integrated into the same module as the detector.

In conclusion, the future of fNIRS and DOT is bound to new silicon technologies, such as SiPMs, VCSELs, and timing circuits, and mass production of components is essential to ensure a wider distribution of the systems at an affordable cost. The work presented here demonstrates that this is already feasible.

ACKNOWLEDGMENTS

This work was supported by the EPSRC-funded UCL Centre for Doctoral Training in Intelligent, Integrated Imaging in Healthcare (i4health) (Grant No. EP/S021930/1) and the Department of Health's NIHR funded Biomedical Research Centre at University College London Hospitals.

The authors would like to thank Arihant Bijjala for building the phantom, Ioana Albu for printing the probes, Diana Sakaan for performing a Monte Carlo simulation, and Dr. Danial Chitnis for recommending the use of the TDC7201.

AUTHOR DECLARATIONS

Conflict of Interest

The authors declare no conflict of interest.

DATA AVAILABILITY

The data that support the findings of this study are openly available in UCL's Figshare repository at <https://figshare.com/s/4c754a417f61a899021b>.²⁹

REFERENCES

- 1 A. P. Gibson, J. C. Hebden, and S. R. Arridge, "Recent advances in diffuse optical imaging," *Phys. Med. Biol.* **50**, R1–R43 (2005).
- 2 A. Pifferi, D. Contini, A. D. Mora, A. Farina, L. Spinelli, and A. Torricelli, "New frontiers in time-domain diffuse optics, a review," *J. Biomed. Opt.* **21**, 091310 (2016).
- 3 F. Lange and I. Tachtsidis, "Clinical brain monitoring with time domain NIRS: A review and future perspectives," *Appl. Sci.* **9**, 1612 (2019).

- 4 A. Dalla Mora, L. Di Sieno, A. Behera, P. Taroni, D. Contini, A. Torricelli, and A. Pifferi, "The SiPM revolution in time-domain diffuse optics," *Nucl. Instrum. Methods Phys. Res., Sect. A* **978**, 164411 (2020).
- 5 H. Wabnitz, D. R. Taubert, M. Mazurenka, O. Steinkellner, A. Jelzow, R. Macdonald, D. Milej, P. Sawosz, M. Kacprzak, A. Liebert, R. Cooper, J. Hebden, A. Pifferi, A. Farina, I. Bargigia, D. Contini, M. Caffini, L. Zucchelli, L. Spinelli, R. Cubeddu, and A. Torricelli, "Performance assessment of time-domain optical brain imagers, part I: Basic instrumental performance protocol," *J. Biomed. Opt.* **19**, 086010 (2014).
- 6 L. Di Sieno, H. Wabnitz, A. Pifferi, M. Mazurenka, Y. Hoshi, A. Dalla Mora, D. Contini, G. Boso, W. Becker, F. Martelli, A. Tosi, and R. Macdonald, "Characterization of a time-resolved non-contact scanning diffuse optical imaging system exploiting fast-gated single-photon avalanche diode detection," *Rev. Sci. Instrum.* **87**, 035118 (2016).
- 7 J. Selb, J. J. Stott, M. A. Franceschini, A. G. Sorensen, and D. A. Boas, "Improved sensitivity to cerebral hemodynamics during brain activation with a time-gated optical system: Analytical model and experimental validation," *J. Biomed. Opt.* **10**, 011013 (2005).
- 8 M. Renna, A. Peruch, Z. Starkweather, J. Sunwoo, and M. A. Franceschini, "Design of a skin-contact sensitive technology for biomedical sensor," *Proc. SPIE* **11633**, 116330D (2021).
- 9 L. Di Sieno, J. Nissinen, L. Hallman, E. Martinenghi, D. Contini, A. Pifferi, J. Kostamovaara, and A. D. Mora, "Miniaturized pulsed laser source for time-domain diffuse optics routes to wearable devices," *J. Biomed. Opt.* **22**, 1 (2017).
- 10 E. Martinenghi, L. Di Sieno, D. Contini, M. Sanzaro, A. Pifferi, and A. Dalla Mora, "Time-resolved single-photon detection module based on silicon photomultiplier: A novel building block for time-correlated measurement systems," *Rev. Sci. Instrum.* **87**, 073101 (2016).
- 11 R. Re, E. Martinenghi, A. D. Mora, D. Contini, A. Pifferi, and A. Torricelli, "Probe-hosted silicon photomultipliers for time-domain functional near-infrared spectroscopy: Phantom and *in vivo* tests," *Neurophotonics* **3**, 045004 (2016).
- 12 M. Buttafava, E. Martinenghi, D. Tamborini, D. Contini, A. D. Mora, M. Renna, A. Torricelli, A. Pifferi, F. Zappa, and A. Tosi, "A compact two-wavelength time-domain NIRS system based on SiPM and pulsed diode lasers," *IEEE Photonics J.* **9**, 7800114 (2017).
- 13 M. Renna, M. Buttafava, A. Behera, M. Zanoletti, L. D. Sieno, A. D. Mora, D. Contini, and A. Tosi, "Eight-wavelength, dual detection channel instrument for near-infrared time-resolved diffuse optical spectroscopy," *IEEE J. Sel. Top. Quantum Electron.* **25**, 7201611 (2019).
- 14 S. Burri, C. Bruschini, and E. Charbon, "A compact linear SPAD camera system with 64 FPGA-based TDC modules for versatile 50 ps resolution time-resolved imaging," *Instruments* **1**, 6 (2017).
- 15 S. Saha, Y. Lu, F. Lesage, and M. Sawan, "Wearable SiPM-based NIRS interface integrated with pulsed laser source," *IEEE Trans. Biomed. Circuits Syst.* **13**, 1313–1323 (2019).
- 16 S. Saha, S. Burri, C. Bruschini, E. Charbon, F. Lesage, and M. Sawan, "Time domain NIRS optode based on null/small source-detector distance for wearable applications," in *2019 IEEE Custom Integrated Circuits Conference (CICC)* (IEEE, 2019).
- 17 S. Saha, Y. Lu, S. Weyers, F. Lesage, and M. Sawan, "Compact optical probe for time-resolved NIRS-imaging," *IEEE Sens. J.* **20**, 6101–6113 (2020).
- 18 Kernel Flow, <https://www.kernel.com/hello-humanity#Kernel-Flow>, 2020; accessed 10 March 2021.
- 19 M. Alayed, D. Palubiak, and M. Deen, "Characterization of a time-resolved diffuse optical spectroscopy prototype using low-cost, compact single photon avalanche detectors for tissue optics applications," *Sensors* **18**, 3680 (2018).
- 20 C. Bruschini, H. Homulle, and E. Charbon, "Ten years of biophotonics single-photon SPAD imager applications: Retrospective and outlook," *Proc. SPIE* **10069**, 100691S (2017).
- 21 J. M. Pavia, M. Scandini, S. Lindner, M. Wolf, and E. Charbon, "A 1 × 400 backside-illuminated SPAD sensor with 49.7 ps resolution, 30 pJ/sample TDCs fabricated in 3D CMOS technology for near-infrared optical tomography," *IEEE J. Solid-State Circuits* **50**, 2406–2418 (2015).
- 22 C. Zhang, S. Lindner, I. M. Antolovic, J. Mata Pavia, M. Wolf, and E. Charbon, "A 30-frames/s, 252 × 144 SPAD flash LIDAR with 1728 dual-clock 48.8-ps

TDCs, and pixel-wise integrated histogramming,” *IEEE J. Solid-State Circuits* **54**, 1137–1151 (2019).

²³A. T. Erdogan, R. Walker, N. Finlayson, N. Krstajic, G. O. S. Williams, and R. K. Henderson, “A 16.5 giga events/s 1024×8 SPAD line sensor with per-pixel zoomable 50 ps–6.4 ns/bin histogramming TDC,” in *2017 Symposium on VLSI Circuits* (IEEE, 2017).

²⁴A. T. Erdogan, R. Walker, N. Finlayson, N. Krstajic, G. Williams, J. Girkin, and R. Henderson, “A CMOS SPAD line sensor with per-pixel histogramming TDC for time-resolved multispectral imaging,” *IEEE J. Solid-State Circuits* **54**, 1705–1719 (2019).

²⁵F. Nolet, W. Lemaire, F. Dubois, N. Roy, S. Carrier, A. Samson, S. A. Charlebois, R. Fontaine, and J.-F. Pratte, “256 pixelated SPAD readout ASIC with in-pixel TDC and embedded digital signal processing for uniformity and skew correction,” *Nucl. Instrum. Methods Phys. Res., Sect. A* **949**, 162891 (2020).

²⁶E. Conca, V. Sesta, M. Buttafava, F. Villa, L. D. Sieno, A. D. Mora, D. Contini, P. Taroni, A. Torricelli, A. Pifferi, F. Zappa, and A. Tosi, “Large-area, fast-gated digital SiPM with integrated TDC for portable and wearable time-domain NIRS,” *IEEE J. Solid-State Circuits* **55**, 3097–3111 (2020).

²⁷R. J. Cooper, E. Magee, N. Everdell, S. Magazov, M. Varela, D. Airantzis, A. P. Gibson, and J. C. Hebden, “MONSTIR II: A 32-channel, multispectral, time-resolved optical tomography system for neonatal brain imaging,” *Rev. Sci. Instrum.* **85**, 053105 (2014).

²⁸K. I. Papadimitriou, L. A. Dempsey, J. C. Hebden, S. R. Arridge, and S. Powell, “A spread spectrum approach to time-domain near-infrared diffuse optical imaging using inexpensive optical transceiver modules,” *Biomed. Opt. Express* **9**, 2648 (2018).

²⁹P. Pérez-Tirador (2021). “Development of a portable time-domain system for diffuse optical tomography of the newborn infant brain,” Figshare. <https://figshare.com/s/4c754a417f61a899021b>.